

See discussions, stats, and author profiles for this publication at: <https://www.researchgate.net/publication/23443505>

# Electrolyte Gating in Redox-Active Tunneling Junctions—An Electrochemical STM Approach

ARTICLE *in* JOURNAL OF THE AMERICAN CHEMICAL SOCIETY · DECEMBER 2008

Impact Factor: 12.11 · DOI: 10.1021/ja8054194 · Source: PubMed

---

CITATIONS

75

---

READS

62

3 AUTHORS, INCLUDING:



Ilya Pobelov

Universität Bern

40 PUBLICATIONS 964 CITATIONS

SEE PROFILE



Zhihai Li

Ball State University

27 PUBLICATIONS 675 CITATIONS

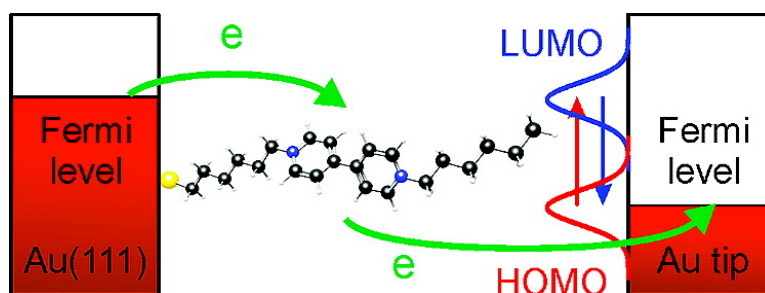
SEE PROFILE

## Electrolyte Gating in Redox-Active Tunneling Junctions#An Electrochemical STM Approach

Ilya V. Pobelov, Zhihai Li, and Thomas Wandlowski

*J. Am. Chem. Soc.*, **2008**, 130 (47), 16045-16054 • Publication Date (Web): 01 November 2008

Downloaded from <http://pubs.acs.org> on December 2, 2008



### More About This Article

Additional resources and features associated with this article are available within the HTML version:

- Supporting Information
- Access to high resolution figures
- Links to articles and content related to this article
- Copyright permission to reproduce figures and/or text from this article

[View the Full Text HTML](#)



ACS Publications  
High quality. High impact.

Electrolyte Gating in Redox-Active Tunneling Junctions—  
An Electrochemical STM ApproachIlya V. Pobelov,<sup>†,‡</sup> Zhihai Li,<sup>†</sup> and Thomas Wandlowski<sup>\*,†,‡</sup>

Department of Chemistry and Biochemistry, University of Bern, CH-3012 Bern, Switzerland, and  
Institute of Bio- and Nanosystems IBN 3 and Center of Nanoelectronic Systems for Informational  
Technology, Research Center Jülich, D-52425 Jülich, Germany

Received July 13, 2008; E-mail: thomas.wandlowski@dcf.unibe.ch

**Abstract:** We report on the construction of an asymmetric tunneling junction between a Au STM tip and a Au(111)–(1 × 1) substrate electrode modified with the redox-active molecule *N*-hexyl-*N'*-(6-thiohexyl)-4,4'-bipyridinium bromide (HS6V6) in an electrochemical environment. The experiments focused on the reversible one-electron transfer reaction between the viologen dication V<sup>2+</sup> and the radical cation V<sup>•+</sup>. Employing the concept of “electrolyte gating” we demonstrate transistor- and diodelike behavior based on in situ scanning tunneling spectroscopy at constant or variable bias voltages. We derived criteria and verified that the experimental data could be represented quantitatively by a model assuming a two-step electron transfer with partial vibrational relaxation. The analysis illustrates that the magnitude of the tunneling enhancement depends on the initial redox state of HS6V6 (V<sup>2+</sup> or V<sup>•+</sup>). Characteristic parameters, such as reorganization energy, potential drop, and overpotential across the tunneling gap were estimated and discussed. We present a clear discrimination between the redox-mediated enhanced and the off-resonance tunneling currents *I*<sub>enh</sub> respective *I*<sub>r</sub> and distinguish between electron transfer in symmetric and asymmetric Au | redox-molecule | Au configurations.

## 1. Introduction

The ability to control charge transport across nanometer-scale metal | molecule | metal junctions represents a key step toward the realization of molecular-based electronics.<sup>1–3</sup> Various experimental approaches have been employed to study molecular junctions in two- and three-terminal configurations. These include scanning probe microscopies (STM, STS, CP-AFM),<sup>4–19</sup>

crossed-wire junctions,<sup>20</sup> mechanical<sup>21–26</sup> and electromigration<sup>27,28</sup> break junctions, nanopores,<sup>29</sup> and mercury drop electrodes.<sup>30</sup> Approaches in condensed media, and in particular in an electrochemical environment, offer unique opportunities to *measure* and to *control* charge transport across single molecule junctions.<sup>2</sup> The measured current reflects both the electrical contact to the external circuit<sup>19</sup> and the functional state of the tailored molecule.

<sup>†</sup> University of Bern.<sup>‡</sup> Institute of Bio- and Nanosystems IBN 3 and Center of Nanoelectronic Systems for Informational Technology.

- (1) Aviram, A.; Ratner, M. A. *Chem. Phys. Lett.* **1974**, *29*, 277–283.
- (2) Tao, N. J. *Nat. Nanotechnol.* **2006**, *1*, 173–181.
- (3) Chen, F.; Hihath, J.; Huang, Z.; Li, X.; Tao, N. *Annu. Rev. Phys. Chem.* **2007**, *58*, 535–564.
- (4) Donhauser, Z. J.; Mantooth, B. A.; Kelly, K. F.; Bumm, L. A.; Monnell, J. D.; Stapleton, J. J.; Price, D. W., Jr.; Rawlett, A. M.; Allara, D. L.; Tour, J. M.; Weiss, P. S. *Science* **2001**, *292*, 2303–2307.
- (5) Andres, R. P.; Datta, S.; Janes, D. B.; Kubiak, C. P.; Reifenger, R. In *Handbook of Nanostructured Materials and Nanotechnology*; Nalwa, H. S., Ed.; AP: New York, 2001; Vol. 3, p 180.
- (6) Gimzewski, J. K.; Joachim, C. *Science* **1999**, *283*, 1683–1688.
- (7) Lu, X.; Hipps, K. W.; Wang, X. D.; Mazur, U. *J. Am. Chem. Soc.* **1996**, *118*, 7197–7202.
- (8) Scudiero, L.; Barlow, D. E.; Hipps, K. W. *J. Phys. Chem. B* **2000**, *104*, 11899–11905.
- (9) Scudiero, L.; Barlow, D. E.; Mazur, U.; Hipps, K. W. *J. Am. Chem. Soc.* **2001**, *123*, 4073–4080.
- (10) Scudiero, L.; Barlow, D. E.; Hipps, K. W. *J. Phys. Chem. B* **2002**, *106*, 996–1003.
- (11) Repp, J.; Meyer, G.; Paavilainen, S.; Olsson, F. E.; Persson, M. *Science* **2006**, *312*, 1196–1199.
- (12) Temirov, R.; Lassise, A.; Anders, B.; Tautz, F. S. *Nanotechnology* **2008**, *19*, 065401.
- (13) Wold, D. J.; Haag, R.; Rampi, M. A.; Frisbie, C. D. *J. Phys. Chem. B* **2002**, *106*, 2813–2816.

- (14) Cui, X. D.; Primak, A.; Zarate, X.; Tomfohr, J.; Sankey, O. F.; Moore, A. L.; Moore, T. A.; Gust, D.; Harris, G.; Lindsay, S. M. *Science* **2001**, *294*, 571–574.
- (15) Fan, F.-R. F.; Yang, J.; Cai, L.; Price, D. W., Jr.; Dirk, S. M.; Kosynkin, D. V.; Yao, Y.; Rawlett, A. M.; Tour, J. M.; Bard, A. J. *J. Am. Chem. Soc.* **2002**, *124*, 5550–5560.
- (16) Xu, B.; Tao, N. J. *Science* **2003**, *301*, 1221–1223.
- (17) Huang, Z.; Chen, F.; D'agosta, R.; Bennett, P. A.; Di Ventra, M.; Tao, N. *Nat. Nanotechnol.* **2007**, *2*, 698–703.
- (18) Tao, N. J. *Phys. Rev. Lett.* **1996**, *76*, 4066–4069.
- (19) Li, C.; Pobelov, I.; Wandlowski, T.; Bagrets, A.; Arnold, A.; Evers, F. *J. Am. Chem. Soc.* **2008**, *130*, 318–326.
- (20) Seferos, D. S.; Trammell, S. A.; Bazan, G. C.; Kushmerick, J. G. *Proc. Natl. Acad. Sci. U.S.A.* **2005**, *102*, 8821–8825.
- (21) Reed, M. A.; Zhou, C.; Muller, C. J.; Burgin, T. P.; Tour, J. M. *Science* **1997**, *278*, 252–254.
- (22) Kergueris, C.; Bourgoin, J.-P.; Palacin, S.; Esteve, D.; Urbina, C.; Magoga, M.; Joachim, C. *Phys. Rev. B* **1999**, *59*, 12505–12513.
- (23) Reichert, J.; Ochs, R.; Beckmann, D.; Weber, H. B.; Mayor, M.; v. Löhneysen, H. *Phys. Rev. Lett.* **2002**, *88*, 176804.
- (24) González, M. T.; Wu, S.; Huber, R.; van der Molen, S. J.; Schönenberger, C.; Calame, M. *Nano Lett.* **2006**, *6*, 2238–2242.
- (25) Huber, R.; González, M. T.; Wu, S.; Langer, M.; Grunder, S.; Horhoiu, V.; Mayor, M.; Bryce, M. R.; Wang, C.; Jitchati, R.; Schönenberger, C.; Calame, M. *J. Am. Chem. Soc.* **2008**, *130*, 1080–1084.
- (26) Lörtscher, E.; Cizek, J. W.; Tour, J.; Riel, H. *Small* **2006**, *2*, 973–977.

Employing in situ STM or a planar nanogap electrode configuration and the concept of “electrolyte gating”,<sup>18,30–35</sup> several groups demonstrated in pioneering studies transistor- and diodelike functions with high current amplification and rectification ratios.<sup>36–45</sup> Examples include porphyrins,<sup>18,46</sup> viologen-type molecular wires,<sup>39,42,47,48</sup> aniline and thiophene oligomers,<sup>36–38,49,50</sup> transition metal complexes,<sup>41,51,52</sup> carotenes,<sup>53</sup> nitro-derivatives of oligophenylene, ethynylene,<sup>54,55</sup> and ferrocene,<sup>56,57</sup> perylene tetracarboxylic diimide,<sup>43–45</sup> and

the redox protein azurin.<sup>40,58–60</sup> The first systematic studies with substituted aliphatic  $\alpha,\omega$ -alkane derivatives by Leary et al.<sup>61</sup> and Chen et al.<sup>62</sup> and those with aromatic 1,4-diaminobenzene-type molecular wires by Venkataraman et al.<sup>63</sup> at solid | liquid interfaces illustrated the possibility of chemical control.

Kuznetsov and Ulstrup initialized recently a discussion on the importance of conformational dynamics and electrical double layer effects on charge transport characteristics in single metal | redox molecule | metal tunneling junctions.<sup>48,64</sup> Importantly, the electronic levels of (single) redox-species in electrochemical metal | molecule | metal tunneling junctions are strongly coupled to the nuclear environmental motion, extending to both local molecular modes and to the liquid (or solid) electrolyte environment.<sup>59,64,65</sup> The following scenarios of interfacial electron transfer (ET) in a nanoscale electrochemical metal | redox molecule | metal configuration have been proposed:<sup>59,64,65</sup> (1) superexchange via off-resonance levels, (2) resonance tunneling,<sup>66–68</sup> (3) noncoherent two-step electron transfer with complete vibrational relaxation,<sup>69,70</sup> or (4) two-step electron transfer with partial vibrational relaxation<sup>65,71–73</sup> (see section 2). Schmickler<sup>74</sup> and Nitzan<sup>75</sup> considered structural fluctuations and the role of water molecules in the gap. A recent stochastic model of Schmickler and Kuznetsov<sup>76</sup> treats fluctuations of the redox level in the tunneling gap explicitly.

Experimentally accessible relations of (i) the source-drain current (between the two working electrodes) and the bias at fixed potential of one working electrode and of (ii) the source-drain current and the potential of one working electrode at fixed bias provide diagnostic criteria to distinguish between different mechanisms of charge transport.<sup>59,64,65</sup>

We emphasize that the asymmetric configuration should be clearly distinguished from a symmetric Au | molecule | Au configuration with a redox molecule chemically bound to both adjacent electrodes. The latter exhibits modifications of the junction conductance due to structure changes of the redox-

- (27) Park, J.; Pasupathy, A. N.; Goldsmith, J. I.; Chang, C.; Yaish, Y.; Petta, J. R.; Rinkoski, M.; Sethna, J. P.; Abruña, H. D.; McEuen, P. L.; Ralph, D. C. *Nature* **2002**, *417*, 722–725.
- (28) van der Zant, H. S. J.; Osorio, E. A.; Poot, M.; O'Neill, K. *Phys. Stat. Sol. B* **2006**, *243*, 3408–3412.
- (29) Chen, J.; Reed, M. A.; Rawlett, A. M.; Tour, J. M. *Science* **1999**, *286*, 1550–1552.
- (30) Tran, E.; Duati, M.; Whitesides, G. M.; Rampi, M. A. *Faraday Discuss.* **2006**, *131*, 197–203.
- (31) White, H. S.; Kittleson, G. P.; Wrighton, M. S. *J. Am. Chem. Soc.* **1984**, *106*, 5375–5377.
- (32) Meulenkaamp, E. A. *J. Phys. Chem. B* **1999**, *103*, 7831–7838.
- (33) Krüger, M.; Buitelaar, M. R.; Nussbaumer, T.; Schönenberger, C.; Forró, L. *Appl. Phys. Lett.* **2001**, *78*, 1291–1293.
- (34) Rosenblatt, S.; Yaish, Y.; Park, J.; Gore, J.; Sazonova, V.; McEuen, P. L. *Nano Lett.* **2002**, *2*, 869–872.
- (35) Corni, S. *IEEE Trans. Nanotech.* **2007**, *6*, 561–570.
- (36) He, H.; Zhu, J.; Tao, N. J.; Nagahara, L. A.; Amlani, I.; Tsui, R. *J. Am. Chem. Soc.* **2001**, *123*, 7730–7731.
- (37) He, H. X.; Li, X. L.; Tao, N. J.; Nagahara, L. A.; Amlani, I.; Tsui, R. *Phys. Rev. B* **2003**, *68*, 045302.
- (38) Chen, F.; He, J.; Nuckolls, C.; Roberts, T.; Klare, J. E.; Lindsay, S. *Nano Lett.* **2005**, *5*, 503–506.
- (39) Haiss, W.; van Zalinge, H.; Higgins, S. J.; Bethell, D.; Höbenreich, H.; Schiffrin, D. J.; Nichols, R. J. *J. Am. Chem. Soc.* **2003**, *125*, 15294–15295.
- (40) Alessandrini, A.; Salerno, M.; Frabboni, S.; Facci, P. *Appl. Phys. Lett.* **2005**, *86*, 133902.
- (41) Albrecht, T.; Guckian, A.; Ulstrup, J.; Vos, J. G. *Nano Lett.* **2005**, *5*, 1451–1455.
- (42) Li, Z.; Han, B.; Mészáros, G.; Pobelov, I.; Wandlowski, T.; Błaszczuk, A.; Mayor, M. *Faraday Discuss.* **2006**, *131*, 121–143.
- (43) Xu, B.; Xiao, X.; Yang, X.; Zang, L.; Tao, N. *J. Am. Chem. Soc.* **2005**, *127*, 2386–2387.
- (44) Li, X.; Hihath, J.; Chen, F.; Masuda, T.; Zang, L.; Tao, N. *J. Am. Chem. Soc.* **2007**, *129*, 11535–11542.
- (45) Li, C.; Mishchenko, A.; Li, Z.; Pobelov, I.; Wandlowski, T.; Li, X. Q.; Würthner, F.; Bagrets, A.; Evers, F. *J. Phys.: Condens. Matter* **2008**, *20*, 374122.
- (46) Yoshimoto, S.; Tada, A.; Suto, K.; Narita, R.; Itaya, K. *Langmuir* **2003**, *19*, 672–677.
- (47) Li, Z.; Pobelov, I.; Han, B.; Wandlowski, T.; Błaszczuk, A.; Mayor, M. *Nanotechnology* **2007**, *18*, 044018.
- (48) Haiss, W.; Albrecht, T.; van Zalinge, H.; Higgins, S. J.; Bethell, D.; Höbenreich, H.; Schiffrin, D. J.; Nichols, R. J.; Kuznetsov, A. M.; Zhang, J.; Chi, Q.; Ulstrup, J. *J. Phys. Chem. B* **2007**, *111*, 6703–6712.
- (49) He, J.; Chen, F.; Lindsay, S.; Nuckolls, C. *Appl. Phys. Lett.* **2007**, *90*, 072112.
- (50) Xu, B. Q.; Li, X. L.; Xiao, X. Y.; Sakaguchi, H.; Tao, N. *J. Nano Lett.* **2005**, *5*, 1491–1495.
- (51) Albrecht, T.; Guckian, A.; Kuznetsov, A. M.; Vos, J. G.; Ulstrup, J. *J. Am. Chem. Soc.* **2006**, *128*, 17132–17138.
- (52) Albrecht, T.; Moth-Poulsen, K.; Christensen, J. B.; Hjelm, J.; Bjørnholm, T.; Ulstrup, J. *J. Am. Chem. Soc.* **2006**, *128*, 6574–6575.
- (53) Visoly-Fisher, I.; Daie, K.; Terazono, Y.; Herrero, C.; Fungo, F.; Otero, L.; Durantini, E.; Silber, J. J.; Sereno, L.; Gust, D.; Moore, T. A.; Moore, A. L.; Lindsay, S. M. *Proc. Natl. Acad. Sci. U.S.A.* **2006**, *103*, 8686–8690.
- (54) Xiao, X.; Nagahara, L. A.; Rawlett, A. M.; Tao, N. *J. Am. Chem. Soc.* **2005**, *127*, 9235–9240.
- (55) He, J.; Fu, Q.; Lindsay, S.; Cizek, J. W.; Tour, J. M. *J. Am. Chem. Soc.* **2006**, *128*, 14828–14835.
- (56) Wassel, R. A.; Credo, G. M.; Fuierer, R. R.; Feldheim, D. L.; Gorman, C. B. *J. Am. Chem. Soc.* **2004**, *126*, 295–300.
- (57) Xiao, X.; Brune, D.; He, J.; Lindsay, S.; Gorman, C. B.; Tao, N. *Chem. Phys.* **2006**, *326*, 138–143.
- (58) Chi, Q.; Farver, O.; Ulstrup, J. *Proc. Natl. Acad. Sci. U.S.A.* **2005**, *102*, 16203–16208.
- (59) Alessandrini, A.; Corni, S.; Facci, P. *Phys. Chem. Chem. Phys.* **2006**, *8*, 4383–4397.
- (60) Chi, Q.; Zhang, J.; Jensen, P. S.; Christensen, H. E. M.; Ulstrup, J. *Faraday Discuss.* **2006**, *131*, 181–195.
- (61) Leary, E.; Higgins, S. J.; van Zalinge, H.; Haiss, W.; Nichols, R. J. *Chem. Commun.* **2007**, 3939–3941.
- (62) Chen, F.; Li, X.; Hihath, J.; Huang, Z.; Tao, N. *J. Am. Chem. Soc.* **2006**, *128*, 15874–15881.
- (63) Venkataraman, L.; Park, Y. S.; Whalley, A. C.; Nuckolls, C.; Hybertsen, M. S.; Steigerwald, M. L. *Nano Lett.* **2007**, *7*, 502–506.
- (64) Kuznetsov, A. M.; Medvedev, I. G.; Ulstrup, J. *J. Chem. Phys.* **2007**, *127*, 104708.
- (65) Zhang, J.; Chi, Q.; Kuznetsov, A. M.; Hansen, A. G.; Wackerbarth, H.; Christensen, H. E. M.; Andersen, J. E. T.; Ulstrup, J. *J. Phys. Chem. B* **2002**, *106*, 1131–1152.
- (66) Schmickler, W.; Widrig, C. *J. Electroanal. Chem.* **1992**, *336*, 213–221.
- (67) Schmickler, W. *Surf. Sci.* **1993**, *295*, 43–56.
- (68) Schmickler, W.; Tao, N. *Electrochim. Acta* **1997**, *42*, 2809–2815.
- (69) Kuznetsov, A. M.; Ulstrup, J. *Chem. Phys.* **1991**, *157*, 25–33.
- (70) Kuznetsov, A. M.; Ulstrup, J. *Surf. Coat. Technol.* **1994**, *67*, 193–200.
- (71) Kuznetsov, A. M.; Ulstrup, J. *J. Phys. Chem. A* **2000**, *104*, 11531–11540.
- (72) Zhang, J.; Kuznetsov, A. M.; Ulstrup, J. *J. Electroanal. Chem.* **2003**, *541*, 133–146.
- (73) Zhang, J.; Chi, Q.; Albrecht, T.; Kuznetsov, A. M.; Grubb, M.; Hansen, A. G.; Wackerbarth, H.; Welinder, A. C.; Ulstrup, J. *Electrochim. Acta* **2005**, *50*, 3143–3159.
- (74) Schmickler, W. *Surf. Sci.* **1995**, *335*, 416–421.
- (75) Nitzan, A. *Annu. Rev. Phys. Chem.* **2001**, *52*, 681–750.
- (76) Kuznetsov, A. M.; Schmickler, W. *Chem. Phys.* **2002**, *282*, 371–377.

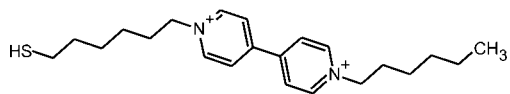


Figure 1. Structure of HS6V6.

active unit, while the former exhibits an enhancement of the tunneling current due to the tuning of the metallic and molecular energy levels with dominant contributions of the solvent dynamics. A maximum of the enhanced tunneling current is often observed when the substrate and tip potentials,  $E_t$  and  $E_s$ , are close to the equilibrium potential  $E^0$  of the corresponding redox pair. This effect was demonstrated for the viologen moieties,<sup>42</sup> derivatives of ferrocene,<sup>56</sup> organometallic complexes,<sup>41,51,52,77</sup> and porphyrins<sup>18</sup> respective metalloproteins.<sup>40,58–60</sup> To the best of our knowledge, we report in this paper the first quantitative scanning tunneling spectroscopy study of a redox active molecule in an asymmetric electrochemical tunneling junction, which is rigorously compared with theoretical predictions based on phenomenological models.

The present paper represents a comprehensive electrochemical study on the tunneling enhancement in an asymmetric configuration between an adsorbate-free Au STM tip and a Au(111)–(1 × 1) substrate electrode modified with chemically bound *N*-hexyl-*N'*-(6-thiohexyl)-4,4'-bipyridinium bromide (HS6V6), which is composed of the redox-active 4,4'-bipyridinium cation  $V^{2+}$  (viologen) as a core, two flexible alkyl spacer units attached to each ring nitrogen, and one terminal SH anchoring group (see Figure 1). The latter ensures the chemical surface immobilization.

We have chosen HS6V6 because the viologen core ( $V^{2+}$ ) is easily reduced forming the radical-cation ( $V^{+\bullet}$ ) and the neutral form ( $V^0$ ).<sup>78–80</sup> The first oxidation–reduction  $V^{2+} \rightleftharpoons V^{+\bullet}$  is completely reversible in bulk solutions as well as immobilized on various surfaces. The redox-active unit has been incorporated as “backbone” component in self-assembled monolayers,<sup>81–84</sup> in a nanometer-scale electronic switch<sup>85</sup> and in various functional materials.<sup>86,87</sup> For a detailed characterization of the macroscopic electrochemical and structure properties of the various viologen-type adlayers on solid electrodes we refer to refs 42 and 88 and the literature cited therein.

The Liverpool group recently pioneered electron transport studies with single molecule wires containing the  $V^{2+}$  core unit, bound symmetrically between the tip of an STM and a gold

substrate.<sup>39,85,89,90</sup> This work was extended by our group in a strictly controlled oxygen-free electrochemical environment and combined with in situ structure studies.<sup>42,47,88</sup> On the basis of the statistical analysis of a large number of current–distance ( $I_T$ – $\Delta z$ ) and current–time ( $I_T$ – $t$ ) traces, both groups demonstrated that the junction conductance increases upon the potential-induced transition from the stable dication  $V^{2+}$  to the radical cation  $V^{+\bullet}$  state.<sup>39,47,48</sup> On the basis of quantum chemistry electronic structure calculations in combination with a nonequilibrium Greens function approach, Bagrets et al. showed that the origin of the experimentally observed conductance change could be attributed to interactions of the tunneling electron with molecular vibrations.<sup>91</sup> This idea was hypothesized before in ref 39 but not further evaluated.

In comparison to previous work, the present study is focused on a detailed and comprehensive quantitative analysis of electron transfer characteristics in a HS6V6-modified asymmetric tunneling configuration. We present new experimental data for this redox-active system and derived model equations directly accessible for the quantitative comparison with models of interfacial electron transfer in nanoscale electrochemical junctions. We will also discuss the distinct differences to redox-active symmetric tunneling junctions.

The paper is organized as follows. In the next section, we will briefly introduce and discuss the phenomenological models and derive predictions, which could be compared with experimental results. The following section will summarize experimental details. Results of the voltammetric and the in situ STM and STS studies are reported in the section Results and Discussion. The main focus is directed to the quantitative analysis of constant respective variable bias spectroscopy data. The paper ends with the section General Comments and Conclusions.

## 2. Theoretical Model

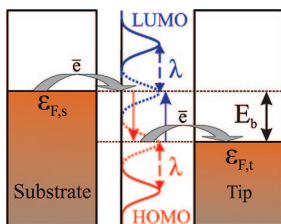
In this section, we summarize the features of the model describing two-step tunneling with partial vibrational relaxation, which was developed by Kuznetsov, Ulstrup, and colleagues,<sup>64,65,69–73,92–96</sup> and derive characteristic dependencies which can be quantitatively compared with our experimental data. We also present a brief comparison to other relevant models. The Kuznetsov–Ulstrup (KU) model is widely applied to rationalize the experimental observations on tunneling enhancement. However, no comprehensive quantitative analysis of experimental data according to this model was carried out so far.

Figure 2 represents a graphic illustration of the KU model. A molecule with discrete electronic levels is located between a metal substrate (for instance Au(111)) and a probe electrode (for instance a Au STM tip), both providing continuously

- (77) Albrecht, T.; Moth-Poulsen, K.; Christensen, J. B.; Guckian, A.; Bjørnholm, T.; Vos, J. G.; Ulstrup, J. *Faraday Discuss.* **2006**, *131*, 265–279.  
 (78) Michaelis, L.; Hill, E. S. *J. Gen. Physiol.* **1933**, *16*, 859–873.  
 (79) Bird, C. L.; Kuhn, A. T. *Chem. Soc. Rev.* **1981**, *10*, 49–82.  
 (80) Monk, P. M. S. *The Viologens*; John Wiley and Sons: Chichester, 1998.  
 (81) Long, H. C. D.; Buttry, D. A. *Langmuir* **1990**, *6*, 1319–1322.  
 (82) Long, H. C. D.; Buttry, D. A. *Langmuir* **1992**, *8*, 2491–2496.  
 (83) Sagara, T.; Kaba, N.; Komatsu, M.; Uchida, M.; Nakashimaa, N. *Electrochim. Acta* **1998**, *43*, 2183–2193.  
 (84) Alvarado, R. J.; Mukherjee, J.; Pacsial, E. J.; Alexander, D.; Raymo, F. M. *J. Phys. Chem. B* **2005**, *109*, 6164–6173.  
 (85) Gittins, D. I.; Bethell, D.; Schiffrin, D. J.; Nichols, R. J. *Nature* **2000**, *408*, 67–69.  
 (86) Lahav, M.; Heleg-Shabtai, V.; Wasserman, J.; Katz, E.; Willner, I.; Dür, H.; Hu, Y.-Z.; Bossmann, S. H. *J. Am. Chem. Soc.* **2000**, *122*, 11480–11487.  
 (87) Akiyama, T.; Inoue, K.; Kuwahara, Y.; Niidome, Y.; Terasaki, N.; Nitahara, S.; Yamada, S. *Langmuir* **2005**, *21*, 793–796.  
 (88) Han, B.; Li, Z.; Wandlowski, T.; Błaszczak, A.; Mayor, M. *J. Phys. Chem. C* **2007**, *111*, 13855–13863.

- (89) Haiss, W.; van Zalinge, H.; Höbenreich, H.; Bethell, D.; Schiffrin, D. J.; Higgins, S. J.; Nichols, R. J. *Langmuir* **2004**, *20*, 7694–7702.  
 (90) Haiss, W.; Nichols, R. J.; Higgins, S. J.; Bethell, D.; Höbenreich, H.; Schiffrin, D. J. *Faraday Discuss.* **2004**, *125*, 179–194.  
 (91) Bagrets, A.; Arnold, A.; Evers, F. *J. Am. Chem. Soc.* **2008**, *130*, 9013–9018.  
 (92) Kuznetsov, A. M. *J. Chem. Phys.* **2007**, *127*, 084710.  
 (93) Kuznetsov, A. M.; Ulstrup, J. *J. Chem. Phys.* **2002**, *116*, 2149–2165.  
 (94) Kornyshev, A. A.; Kuznetsov, A. M.; Nielsen, J. U.; Ulstrup, J. *Phys. Chem. Chem. Phys.* **2000**, *2*, 141–144.  
 (95) Friis, E. P.; Kharkats, Y. I.; Kuznetsov, A. M.; Ulstrup, J. *J. Phys. Chem. A* **1998**, *102*, 7851–7859.  
 (96) Kuznetsov, A. M.; Ulstrup, J. *J. Electroanal. Chem.* **2004**, *564*, 209–222.





**Figure 2.** Schematic energy level diagram of a two-step ET process mediated by a redox-active molecule. The electron is transferred from the Fermi level of the substrate (left)  $\epsilon_{F,s}$  to the LUMO of the molecule and after partial vibrational relaxation to the Fermi level of the tip  $\epsilon_{F,t}$  (right).

distributed electronic levels. The localized levels of the molecule are broadened by interactions of the redox-center with the surrounding electrolyte and with the substrate. In an electrochemical environment, the potentials of both electrodes,  $E_s$  and  $E_t$ , are controlled independently with respect to the reference electrode, and their difference determines the bias voltage  $E_b = E_s - E_t$ .

A direct (off-resonant) tunneling current is flowing between the tip and the substrate independently on the relative positions of the molecular levels with respect to the Fermi levels  $\epsilon_{F,s}$  and  $\epsilon_{F,t}$  of the adjacent electrodes. The energy levels of the solvated molecule are constantly fluctuating around their average positions due to variations of the solvation energy up to the value of  $\lambda$  (Gibbs energy of the environmental reorganization). At the first step of the enhanced tunneling, the Fermi level of one of the electrodes (in Figure 2, we consider  $\epsilon_{F,s}$  of the substrate (left) electrode) approaches the lowest unoccupied molecular orbital (LUMO) of the redox species but is still located below it. The LUMO may decrease its energy due to fluctuations and approach the Fermi level of the left electrode,  $\epsilon_{F,s}$ , causing the first ET.

Three scenarios of the second ET are possible. (i) If the electron is transferred “immediately”, i.e., without relaxation of the molecule and of the environment, the process is referred to as a resonant tunneling.<sup>59,66–68</sup> When a reduced center has sufficient time to vibrationally relax, two other situations are possible: (ii) In the diabatic limit (weak electronic coupling between the redox center and both adjacent electrodes), the ET rate is small and the reduced center is completely relaxed vibrationally before the second ET. The second step loses “energy coherency” with the first one, and the reaction path proceeds again via a Franck–Condon barrier. This scenario results in a small current enhancement, as basically only one electron is transferred per initial (first step) molecular fluctuation.<sup>69,70</sup> (iii) We now consider the adiabatic limit (strong electronic coupling between the molecule and both adjacent electrodes)<sup>65,71–73</sup> with a fast ET between the molecule and the electrodes. This situation corresponds to an intermediate case; i.e. two-step ET with partial vibrational relaxation and partial coherence. After the first step, the energy of the now occupied LUMO decreases due to the vibrational relaxation, and the second ET step occurs before complete vibrational relaxation and before the energy of the molecular level passes the Fermi level of the second electrode  $\epsilon_{F,t}$ . Subsequently, the empty LUMO starts to relax toward higher energies and may accept another electron from the left electrode (substrate) before it passes its Fermi level, thus repeating the cycle. The process may comprise many cycles of consecutive molecular reduction and reoxidation steps per single initial fluctuation of the molecular level.

The equations of the model are based on a two-step ET process and may be derived similar to standard equations of electrochemical kinetics in so-called “normal region”.<sup>65</sup> The total enhanced current  $I_{\text{enh}}$  is given by

$$\frac{1}{I_{\text{enh}}} = \frac{1}{I_1} + \frac{1}{I_2} \quad (1)$$

where  $I_1$  and  $I_2$  are the currents due to the substrate–molecule and molecule–tip ETs, respectively.

$$I_1 = e\kappa_1\rho_1(eE_b)\frac{\omega}{2\pi} \exp\left[-\frac{(\lambda + e\xi\eta + e\gamma E_b)^2}{4\lambda kT}\right] \quad (2)$$

$$I_2 = e\kappa_2\rho_2(eE_b)\frac{\omega}{2\pi} \exp\left[-\frac{(\lambda - e\xi\eta - e\gamma E_b + eE_b)^2}{4\lambda kT}\right] \quad (3)$$

Here  $e$  is the elementary charge,  $\kappa$  is the electronic transmission coefficient,  $\rho$  is the density of electronic states in the metal near the Fermi level,  $\omega$  is the characteristic nuclear vibration frequency,  $\eta = E_s - E^0$  is the overpotential,  $k$  is the Boltzmann constant, and  $T$  is the temperature.  $\xi$  and  $\gamma$ , both ranging between 0 and 1, are model parameters describing the shift of the effective electrode potential at the reactive center with the variation of  $\eta$  and  $E_b$ , respectively. They account for the nonlinear potential distribution in the tunneling gap.<sup>71,95,96</sup>

Assuming the same values of  $\kappa$  and  $\rho$  for both ETs, one obtains the following dependence of  $I_{\text{enh}}$  on  $E_b$  and  $\eta$  at a fixed geometry of the tunneling junction (eq 4):

$$I_{\text{enh}} = e\kappa\rho(eE_b)\frac{\omega}{2\pi} \left\{ \exp\left[\frac{e}{4\lambda kT}(\lambda + \xi\eta + \gamma E_b)^2\right] + \exp\left[\frac{e}{4\lambda kT}(\lambda + E_b - \xi\eta - \gamma E_b)^2\right] \right\}^{-1} \quad (4)$$

$$I_{\text{enh}} = 1820E_b \left\{ \exp\left[\frac{9.73}{\lambda}(\lambda + \xi\eta + \gamma E_b)^2\right] + \exp\left[\frac{9.73}{\lambda}(\lambda + E_b - \xi\eta - \gamma E_b)^2\right] \right\}^{-1} \quad (5)$$

Here  $\lambda$  is expressed in volts, which is numerically equal to the energy in electronvolts. With the assumption of  $\kappa = 1$  (i.e., the fully adiabatic limit) and using typical values of  $\omega$  for an aqueous environment and  $\rho$  for gold, one obtains<sup>97</sup>  $A = e^2\rho\omega/(4\pi) = 9.1 \times 10^{-7} \text{ C}^2 \cdot \text{eV}^{-1} \cdot \text{s}^{-1}$ . This leads to a “numerical” version of eq 4 (eq 5) where  $I_{\text{enh}}$  is in nanoamps,  $E_b$  and  $\eta$  are in volts, and  $\lambda$  is in electronvolts.

At low  $\eta$  and  $E_b$  ( $E_b, \eta \ll \lambda$ ), one obtains the “simplified” equation

$$I_{\text{enh}} = \frac{910E_b \exp[-9.73(\lambda + E_b)]}{\cosh[19.4(\xi\eta + (\gamma - 1/2)E_b)]} \quad (6)$$

where  $\cosh(x) \equiv [\exp(x) + \exp(-x)]/2$  is a hyperbolic cosine function. The assumed units are the same as above. Equation 6 represents the theoretically predicted shape of the  $(I_{\text{enh}} - E_s)_{E_b}$  dependence:

$$I_{\text{enh}}(E_s) = I_{\text{peak}}/\cosh[w(E_s - E_{\text{peak}})] \quad (7)$$

where  $I_{\text{peak}} = 910E_b \exp[-9.73(\lambda + E_b)]$  and  $E_{\text{peak}} = E^0 + (1/2 - \gamma)E_b/\xi$  are height and position of the enhanced current peak, respectively. The expression  $w = 19.4\xi$  describes the width of the peak. A higher value of  $w$  represents a narrower peak.

On the basis of eqs 6 and 7, two important correlations can be derived. First, the slope of the  $E_{\text{peak}}$  vs  $E_b$  dependence is

(97) Albrecht, T.; Guckian, A.; Ulstrup, J.; Vos, J. *IEEE Trans. Nanotech.* **2005**, *4*, 430–434.

$(1/2 - \gamma)/\xi$ , and the intercept with the ordinate axis is given by  $E^0$ . Second, the dependence of  $I_{\text{peak}}$  on  $E_b$  may be expressed as

$$\ln(I_{\text{peak}}/E_b) = (6.81 - 9.73\lambda) - 9.73E_b \quad (8)$$

The slope of the  $\ln(I_{\text{peak}}/E_b)$  vs  $E_b$  dependence represents a second relation to compare experimental data with theoretical predictions. The intercept with the ordinate allows to estimate the reorganization energy  $\lambda$ . The latter characterizes the dynamics of nuclear modes coupled with the ET in solution and may be evaluated by a number of experimental and theoretical methods. To our knowledge, the correlation given by eq 8 is described for the first time.

As we will show in sections 4.3 and 4.4, the model just presented describes our experimental data quantitatively. However, we also considered alternative approaches, such as resonant tunneling<sup>59,66–68</sup> and a vibrationally coherent two-step ET.<sup>98</sup> The applicability of the respective models can be tested by a simple criterion. According to the KU model with partial vibrational relaxation and coherence, the enhanced tunneling current at constant and low bias voltage peaks close to  $E^0$  (cf. eq 7). The two other models predict a maximum as well, but it is shifted from  $E^0$  approximately by the value of the reorganization energy  $\lambda$ .<sup>60,71</sup> The latter has typical values of a few hundred millielectronvolts, and the shift may be clearly observed in the experimental data. The stochastic adiabatic model<sup>76</sup> seems to predict a peak around  $E^0$  as well, but does not provide an analytical solution directly applicable for comparison to experimental data. Finally, the model of noncoherent two-step ET with complete vibrational relaxation will lead to a weak, hardly detectable enhancement of the tunneling current in the present configuration.<sup>65,69,70</sup>

### 3. Experimental Section

The electrolyte solutions were prepared with Milli-Q water (18.2 M, 2 ppb TOC), HCl (35%, Merck suprapure), NaOH (Merck, suprapure), KClO<sub>4</sub>, and LiClO<sub>4</sub> (Fluka puriss. p.a., twice recrystallized from Milli-Q water). The synthesis of *N*-hexyl-*N'*-(6-thiohexyl)-4,4'-bipyridinium bromide (HS6V6) and its assembly on Au(111)–(1 × 1) electrodes were described before.<sup>42,47,88</sup>

The current–voltage EC STS experiments were carried out with high coverage self-assembled monolayers (SAMs) of HS6V6 on a disk-shaped (diameter ca. 10 mm) Au(111) electrode in 0.5 M LiClO<sub>4</sub> (pH adjusted to ca. 8.5 by addition of NaOH). We have chosen the high ionic strength in the STS experiments to reduce distortions of the experimental current–voltage traces due a high solution resistance. The tips were electrochemically etched gold wires (0.25 mm diameter) coated with polyethylene. Silver and platinum wires were used as quasi-reference electrode (QRE) and counter electrode, respectively. The potential of the QRE was calibrated with respect to a saturated calomel electrode (SCE). All electrode potentials given in this paper refer to the SCE. An oxygen-free environment was created using an argon-filled all-glass chamber, which hosted the entire electrochemical STM stage. Cyclic voltammograms were regularly recorded in the STM cell prior to the EC STS experiments and between series of measurements to monitor the equilibrium potential of the viologen redox couple  $E^0$ , the quality and stability of the monolayer, and to ensure the absence of oxygen. Complementary STM imaging experiments were carried out under the same or under slightly modified conditions (solution 0.05 M KClO<sub>4</sub>, adjusted to pH  $\approx$  7 by KOH, tungsten tips).<sup>42,47</sup>

To record a single current–voltage curve, the lateral scanning was stopped and subsequently the Au tip was stabilized via the STM feedback loop. The tip–substrate separation was thus

controlled by selected initial values of the bias voltage  $E_b$  and of the tunneling current  $I_{T0}$ . The tunneling current was than recorded in a potential cycle at a fixed geometry of the tunneling junction with the feedback being temporarily switched off. In constant bias mode the bias voltage was fixed, while both  $E_t$  and  $E_s$  were cycled with a rate of  $0.5 \text{ V} \cdot \text{s}^{-1}$ . In variable bias mode,  $E_s$  was fixed and  $E_t$  was cycled in a wide potential range with a rate of  $0.5\text{--}2 \text{ V} \cdot \text{s}^{-1}$ . In both cases the initial values of  $E_s$  and  $E_t$  were sufficiently far away from  $E^0$ . The experiment was repeated 5–10 times for every set of experimental conditions.

The EC STS experiments require a high stability of the tip position. The lateral tip stability and the high quality of the Au STM tip were checked by monitoring in situ STM images after every sequence of current–voltage data. The vertical stability was checked by disabling the feedback loop and observing the evolution of the tunneling current. The EC STS measurements were carried out only if the tip displacement was negligible compared to the recording time of a complete current–voltage trace (1–5 s). Only scans showing a return of  $I_T$  to the initial setpoint current  $I_{T0}$ , after completion of one cycle, were selected for the further analysis.

Comparative “blank” spectroscopy experiments were also conducted to evaluate the contribution of the electrochemical (“leakage”) current to the overall tip signal. These experiments revealed that this faradaic contribution is negligible in all experiments presented.

The data recorded in constant bias mode showed no significant differences between the forward and the backward scans. The curves shown in this paper were obtained by averaging 10–20 individual forward and backward scans of sweeps recorded under identical conditions.

The correlation plots (Figures 6 and 7) were constructed by extracting  $E_{\text{peak}}$  and  $I_{\text{peak}}$  from individual scans and averaging the values corresponding to the given conditions (see main text). The error bars on the plots represent the standard deviation.

A small hysteresis was found on the curves recorded in variable bias mode due to instrumental distortions. It was eliminated by averaging the forward and the backward scans of one sweep. The obtained average curves display no systematic effect of the voltage sweep rate. A representative “master curve” (Figure 9) was constructed by averaging 12 individual scans representing different values of scan rates ranging between 0.5 and  $2.0 \text{ V} \cdot \text{s}^{-1}$ .

### 4. Results and Discussion

**4.1. Electrochemistry of HS6V6 Adlayer.** Figure 3 shows typical cyclic voltammograms (CVs) of an HS6V6 monolayer on Au(111)–(1 × 1) in 0.05 M KClO<sub>4</sub> with the pH adjusted to 10 as recorded in an electrochemical glass cell with the electrode in a hanging meniscus configuration.<sup>42,47,88</sup> Figure 3A represents

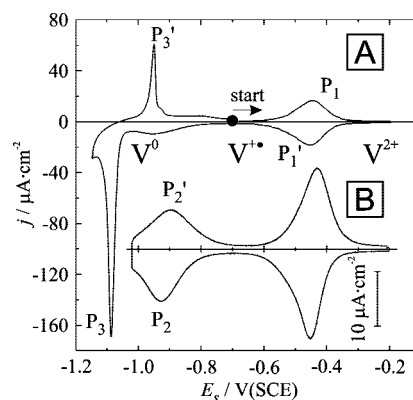


**Figure 3.** Cyclic voltammograms of a high coverage adlayer ( $\Gamma = 3.3 \times 10^{-10} \text{ mol} \cdot \text{cm}^{-2}$ ) of HS6V6 on Au(111)–(1 × 1) in 0.05 M KClO<sub>4</sub> with a sweep rate of  $50 \text{ mV} \cdot \text{s}^{-1}$ . Characteristic peaks and potential regions are indicated (see text).

(98) Kuznetsov, A. M.; Ulstrup, J. *Electrochim. Acta* **2000**, *45*, 2339–2361.

the first CV scan of a freshly prepared electrode from  $E_s = -0.70$  to  $-0.20$  V, then to  $-1.3$  V, and subsequently back to the initial value. The excursion of the substrate potential in this range reveals three characteristic pairs of current peaks labeled  $P_1/P_1'$ ,  $P_2/P_2'$ , and  $P_3/P_3'$ . The latter corresponds to the irreversible reductive desorption and a partial oxidative readsorption of the redox-active thiolate.  $P_1/P_1'$  and  $P_2/P_2'$  represent the two one-electron redox reactions of the surface confined viologen unit,  $V^{2+} \rightleftharpoons V^{+\bullet}$  and  $V^{+\bullet} \rightleftharpoons V^0$ , respectively. Figure 3B shows an enlargement of this region restricting the potential range to  $E_s \geq -1.05$  V. The stability regions of HS6V6 in the three redox states are also indicated. The peak-to-peak separation of  $P_1/P_1'$  is small and almost constant up to a sweep rate of  $1 \text{ V} \cdot \text{s}^{-1}$  indicating a rather fast ET. The peak heights scale linearly with scan rate. The equilibrium potential  $E^0$  of the redox pair  $V^{2+}/V^{+\bullet}$  was estimated as the midpoint between the peaks  $P_1$  and  $P_1'$ . In comparison with the latter, the peaks  $P_2/P_2'$  are broader and their separation is larger. These observations indicate a slower ET.<sup>42</sup> We notice that similar cyclic voltammograms as shown in Figure 3 were also recorded in our STM setup prior to the EC STS measurements.

**4.2. Structure of HS6V6 Adlayers.** A series of EC STM experiments was carried out at potentials around the first pair of redox peaks,  $P_1/P_1'$ , to explore the respective HS6V6 adlayers on Au(111)-(1 × 1).<sup>42,47</sup> Depending on the assembly conditions, two different structures were obtained:

A highly ordered low coverage adlayer of HS6V6 features regular arrays of parallel stripes covering the entire substrate surface (Figure 4A). The stripes are not uniform. Bright and dark contrast patterns alternate. Individual domains extend from 10 to 50 nm. Neighboring domains with sharp boundaries are mutually rotated by multiples of  $120^\circ$  indicating registry of the adlayer with respect to the hexagonal substrate surface. This hypothesis is also supported by the faceting of steps (Figure 4A). The steps are aligned with characteristic angles of  $120^\circ$ , and step edges are decorated by parallel molecular rows.

High-resolution experiments, such as those shown in the inset of Figure 4A, reveal more details of the molecular adlayers. The molecular rows are composed of bright dots separated by parallel rows of dark gray and light gray ellipsoidlike segments. Parallel rows of the same type are separated by  $2.6 \pm 0.3$  nm. The axes of two types of rows exhibit characteristic tilt angles with respect to the main row direction, which were estimated to  $60 \pm 5^\circ$  (light gray rows) and  $90 \pm 10^\circ$  (dark gray rows). Cross-section profiles reveal a periodicity of  $0.50 \pm 0.05$  nm between individual features of each type of row. These observations and the comparison with a systematic study of the assembly and surface structure of viologen mono- and dialkyl-dithiols with variable length of the alkyl spacers<sup>42,47</sup> as well as SEIRAS studies<sup>42,88</sup> allowed the deduction of a structure model of the low coverage “striped” phase. The bright features forming a double row pattern were attributed to the thiol groups of adjacent molecules. The dark gray rows represent the methylene chains, and the light gray ellipsoidal features are assigned to the viologen cores.

The high coverage phase is a poorly ordered adlayer with many atomically deep vacancy islands. Their typical diameter varies between 2–5 nm (Figure 4B). A  $(\sqrt{7} \times \sqrt{7})R19.1^\circ$  structure motif could be tentatively identified (inset in Figure 4B). With reference to our recent SEIRAS study,<sup>88</sup> we assign this adlayer to HS6V6 molecules attached to the Au(111) electrode via the HS anchoring group in a tilted orientation.

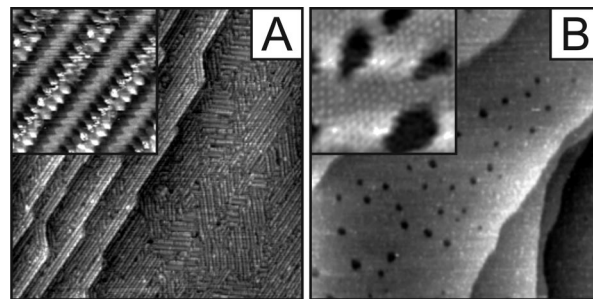


**Figure 4.** STM images of HS6V6 adlayers on Au(111)-(1 × 1) in 0.05 M KClO<sub>4</sub>, pH ≈ 7,  $E_s = -0.2$  V,  $E_b = 0.1$  V,  $I_T = 50 \dots 100$  pA: (A) low coverage,  $\Gamma = 1.2 \times 10^{-10} \text{ mol} \cdot \text{cm}^{-2}$ ,  $100 \times 100$  nm, (inset)  $7 \times 7$  nm; (B) high coverage,  $\Gamma = 3.3 \times 10^{-10} \text{ mol} \cdot \text{cm}^{-2}$ ,  $100 \times 100$  nm, (inset)  $12 \times 12$  nm.

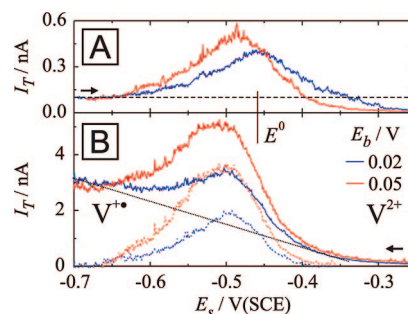


**Figure 5.** Average  $I_T$  vs  $E_s$  curves recorded in constant bias spectroscopy mode,  $I_{T0} = 0.1$  nA. Other experimental conditions are as in Figure 4B. The sweep started in the stability region of  $V^{+\bullet}$  (A) left of  $E^0$  or  $V^{2+}$  (B), right of  $E^0$ . The solid red and blue traces correspond to  $E_b = 0.05$  or  $0.02$  V, respectively. The dashed black line in A represents  $I_{T0}$ . The dotted black line in B is the baseline for the solid curves and the dotted colored lines are the baseline-corrected solid ones.

**4.3. Constant Bias Spectroscopy.** Figure 5 shows selected examples of  $(I - E_s)_{E_b}$  curves. The scans either started at potentials  $E_s < E^0$  (A) or  $E_s > E^0$  (B), corresponding to the HS6V6 in the  $V^{+\bullet}$  or in the  $V^{2+}$  redox state for two different bias voltages  $E_b$ .

The initial part of the curves displays a constant, nonenhanced current, equal to the tunneling setpoint  $I_{T0}$  (dashed black line in the Figure 5A). The latter indicates the temporal stability of the tunneling junction. The current increases in the vicinity of  $E^0$ , reaches a maximum, and finally stabilizes at a constant value.

For fixed gap geometry in the *asymmetric* configuration, the current is higher at the negative tail of the peak. This observation is explained by an increase of the off-resonant ET rate from  $V^{2+}$  to  $V^{+\bullet}$ . The same trend was reported in single molecule electron transport studies with dithiol-functionalized viologen-based molecular wires in a symmetric STM configuration.<sup>39,42,47,48</sup> Gittins et al.<sup>85</sup> reported from current-distance STS measurements a lowering of the tunneling barrier in asymmetric assemblies of viologen-containing junctions which contained a chemically bound gold nanoparticle.

We found that  $I_{\text{peak}}$  was higher when the tip was initially stabilized at  $E_s > E^0$ , compared to starting the STS scan at  $E_s < E^0$ , i.e. in the potential region of  $V^{+\bullet}$  stability (Figure 5). The difference between the respective values of  $I_{\text{peak}}$  reaches up to 1 order of magnitude. These data reflect partially the different off-resonant ET properties of  $V^{2+}$  and  $V^{+\bullet}$ . However, we attribute the main contribution to the fact that tip–substrate separation and tunneling current are not controlled independently. The initial configuration corresponds to a constant



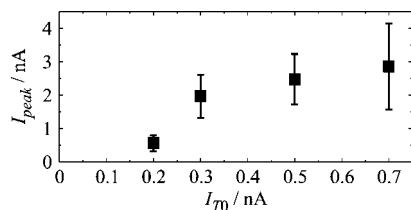


**Figure 6.** Dependence of the peak current  $I_{\text{peak}}$  on the preset tunneling current  $I_{T0}$  obtained from a set of  $I_T$  vs  $E_s$  traces at constant  $E_b = 0.2$  V. The potential sweep started at  $E_s = -0.7$  V, i.e. in the stability region of  $V^{2+}$ . Each data point plotted represents the average of 5–7 traces, in total 25.

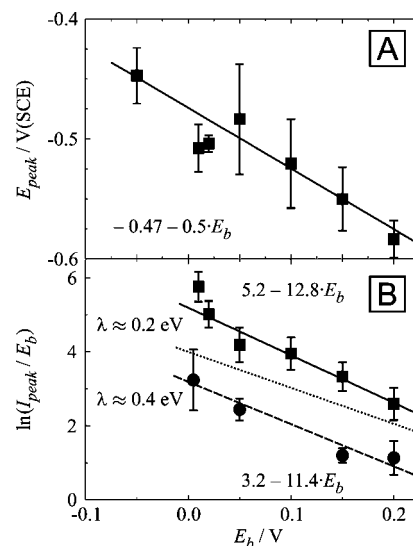
tunneling resistance, rather than to a fixed distance between the Au STM tip and the Au substrate. In consequence, a wider tunneling gap is expected for the more conductive junction at  $E_s < E^0$ . The observed difference in the magnitude of  $I_{\text{peak}}$  corresponds to a higher tunneling current due to a closer proximity of the STM tip to the substrate. This effect is not explicitly described by the KU two-step ET model introduced in section 2, but, as it will be shown below, agrees with it.

Figure 6 illustrates that the enhanced tunneling current  $I_{\text{peak}}$  increases with increasing setpoint current  $I_{T0}$  until it reaches a plateau at  $I_{T0} \geq 0.5$  nA. This trend reflects the following scenario: small setpoint currents correspond to a large tip–molecule distance and, therefore, a small electronic transmission coefficient between tip and molecule. Large values of  $I_{T0}$  represent a small tunneling gap and a large transmission coefficient, which leads to an increase of the tunneling current (cf. eqs 4 and 5 and ref 51). At sufficiently high  $I_{T0}$  (in our case  $I_{T0} \geq 0.5$  nA), the STM tip will eventually contact the molecule, and the substrate–molecule electron transfer will govern the overall tunneling current, which appears to be rather independent of the tip position.

The value of  $E_{\text{peak}}$  was found to be independent of initial potential and/or setpoint current. The  $E_{\text{peak}}$  vs  $E_b$  dependence was constructed by averaging all data for a given bias (Figure 7A). Linear regression yields a slope close to  $-0.5$  and an intercept of  $E_s = -0.47$  V. The proximity of the latter value to  $E^0$  (here  $-0.46$  V) provides strong support for the applicability of the model expressed by eqs 4–7. The expression for the slope contains both  $\xi$  and  $\gamma$ . Therefore, these parameters cannot be evaluated independently. However, if we assume  $\xi \approx 1$ , i.e. a complete “transfer” of the overpotential to the redox center, one obtains as an estimation  $\gamma \approx 1$ .<sup>77</sup>

Figure 7B shows the two  $\ln(I_{\text{peak}}/E_b)$  vs  $E_b$  dependencies (eq 8) extracted from individual traces starting in the stability region of either  $V^{2+}$  or of  $V^{+}$ . The slopes of the linear regressions to the two experimental series are somewhat higher than the one predicted by the KU two-step ET model ( $9.73$  V<sup>−1</sup>; cf. eq 8). However, the agreement is still reasonable. The intercepts provide estimations of the values of the reorganization energy  $\lambda$ . We obtained for the two data sets  $0.2 \pm 0.03$  and  $0.4 \pm 0.03$  eV, respectively. These results do not change significantly if a line with the fixed theoretical slope is fitted to the experimental data. The two values of  $\lambda$  represent in terms of the model the difference between the two starting situations. Similar experimental dependencies of positions and heights of a tunneling resonance on the bias voltage were displayed for azurin in a series of constant bias spectroscopy traces by Alessandrini et al.<sup>40,59</sup> However, no attempts to quantify these observations were reported.

At this stage we emphasize that the correlations suggested by eqs 7 and 8 are only valid strictly in the limit of low  $E_b$  and



**Figure 7.** (A) Dependence of the position of the resonance peak  $E_{\text{peak}}$  on the applied bias as obtained from individual  $I_T$  vs  $E_s$  curves (in total 208; cf. Figure 5). The solid line represents the linear fit to the data shown. (B) Dependence of the height of the resonance peak on the applied bias for curves starting from the  $V^{2+}$  (■: 166 curves) or  $V^{+}$  (●: 48 curves) form. The solid and the dashed lines are linear fits of these groups of points. The dotted line is a guide line with the theoretical slope.

$\eta$  values. However, their sole purpose in the present context is to compare experimental data with the theoretical model on a qualitative and semiquantitative level. As we will demonstrate below, the extracted data are in good agreement with the more detailed analysis.

In addition, we emphasize again that the models introduced in section 2 describe an *enhancement* of the current on top of the contribution due to direct tunneling. Unfortunately, the “switching” of the off-resonant current between  $V^{2+}$  and  $V^{+}$  cannot be investigated independently. One may assume that it will follow the same sigmoid potential dependence as the single molecule transport current measured in a symmetric Au | HS6V6SH | Au configuration under the same conditions.<sup>42</sup> Unfortunately, the exact shape of the curve cannot be evaluated strictly within the present phenomenological approach to ET. It would require input from transport calculations based on an ab initio treatment of the electronic structure of the tunneling junction, which is beyond the scope of the paper.

As an approximation, we performed a linear baseline correction to account for the contribution due to direct tunneling. An example is shown in Figure 5B. The dotted black line represents the interpolated baseline to the solid blue and red curves, and the two dashed colored lines correspond to these solid lines after correction.

The fits of the “full” equation of the tunneling resonance (eq 5) to typical baseline-corrected experimental  $I_T$  vs  $E_s$  curves are shown in Figure 8. The theoretical lines (dotted) reproduce the shape of the original curves rather well. The fit parameters are summarized in Table 1. The same analysis procedure was repeated for the curves measured under other experimental conditions. Independently of the initial redox-form of the viologen core, the values of  $\xi$  and  $\gamma$  were found to be in the range of 0.7–1 and 0.85–1, respectively. Both  $\xi$  and  $\gamma$  slightly decrease upon the increase of the bias voltage. Occasionally, nonphysical values of  $\xi$  and/or  $\gamma > 1$  were obtained (see e.g. results for plot A in Table 1). In this case, the fitting was repeated with those parameters fixed to 1. The shape of the

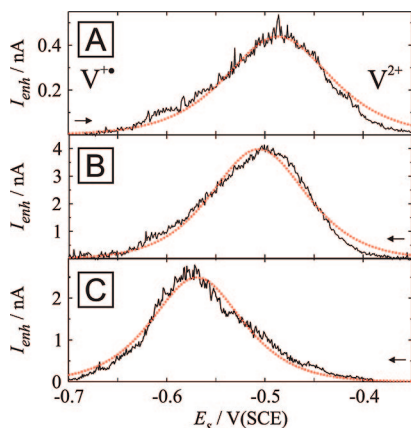


**Figure 8.**  $I_{\text{enh}}$  vs  $E_s$  curves, each is an average of 5–10 individual ones, after baseline correction (solid line; cf. Figure 5). The sweep started from  $V^{+•}$  (A) or  $V^{2+}$  (B and C) adlayers. (A)  $E_b = 0.05$  V,  $I_{T0} = 0.1$  nA; (B)  $E_b = 0.1$  V,  $I_{T0} = 0.1$  nA; (C)  $E_b = 0.2$  V,  $I_{T0} = 0.02$  nA. The dashed curves are fits using the full equation (eq 5) of the resonance peak.

**Table 1.** Model Parameters Obtained for Curves in Figure 8<sup>a</sup>

plot	experimental data			equation 5			equation 6		
	initial form	$E_b$ / V	$I_{T0}$ / nA	$\lambda$ / eV	$\xi$	$\gamma$	$\lambda$ / eV	$\xi$	$\gamma$
A	$V^{+•}$	0.05	0.1	0.42	0.99	1.10	0.42	1.16	1.21
A <sup>b</sup>				0.42	0.94	1	0.43	1	1
B	$V^{2+}$	0.1	0.1	0.21	0.86	0.9	0.22	1.23	1.07
B <sup>b</sup>							0.23	1	1
C	$V^{2+}$	0.2	0.02	0.19	0.75	0.91	0.24	1.30	1.21
C <sup>b</sup>							0.25	1	1

<sup>a</sup> Standard error below 0.01. <sup>b</sup> Fit with fixed values of  $\xi$  and/or  $\gamma$ .

recalculated curves reproduces that of the original experimental curves well (the slight asymmetry of the experimental curves will be addressed in section 5). The obtained values of the reorganization energy  $\lambda$  were 0.2 or 0.4 eV depending on the initial redox form of the viologen. These data are in full agreement with the results of the semiquantitative analysis of the  $\ln(I_{\text{peak}}/E_b)$  vs  $E_b$  dependence (Figure 7B). The variation  $\lambda$  of upon variation of  $E_b$  is negligible and nonsystematic.

Complementary simulations were carried out by using the “simplified” equation (eq 6). The latter is typically used to (semi)quantitatively analyze results of constant bias spectroscopy traces. The simulated curves were found to be very similar to those obtained with the “full” equation. However, the values of all three parameters  $\lambda$ ,  $\xi$ , and  $\gamma$  appear to be slightly overestimated (Table 1). In particular,  $\gamma > 1$  and  $\xi > 1$  were often obtained. Fitting with fixed values  $\xi = \gamma = 1$  did not lead to a significant variation of  $\lambda$  (Table 1), but the shapes of the simulated curves slightly differ from the original ones. We note that the values of  $\xi$  and  $\gamma$ , as determined using both the full and the simplified equations are in agreement with a slope of the  $E_{\text{peak}}$  vs  $E_b$  dependence (Figure 7A) equal to  $-0.5$  (eq 7).

The sequence of plots (A–C) in Figure 8 corresponds to an increasing deviation from the assumption  $E_b \ll \lambda$  used to deduce the simplified equation. Consequently, there is a clear trend in deviations between the parameters as obtained by using the two equations. However, the agreement between these two analysis approaches, as well as with the results extracted from the correlation plots (Figure 7), is still good. Therefore, we conclude that the simplified equation can be used semiquantitatively to analyze the data obtained in constant bias spectroscopy mode.

However, one should bear in mind that this approach leads to an overestimation of all parameters, especially if  $\lambda$  is small and  $E_b$  is high.

**4.4. Variable Bias Spectroscopy.** Complementary EC STS experiments were carried out in variable bias mode with a fixed substrate potential  $E_s = -0.2$  V and a tip potential  $E_t$  varied in a wide range. We ensured that the potential ranges chosen were sufficiently far from the second redox process at  $P_2/P_2'$  (cf. Figure 3).

The resulting  $(I_T - E_t)_{E_s}$  curve (Figure 9) is asymmetric. For  $E_t > E_s$  (i.e.,  $E_b < 0$ ) and at small positive values of  $E_b$ , a nearly linear current response was observed, which is characteristic for direct tunneling at a fixed gap geometry. The dashed line in Figure 9 represents the fit to the linear part. An enhanced exponential-like tunneling response is observed at  $E_t \leq -0.25$  V. The ratio of the tunneling current between the negative and the corresponding positive branches of the  $I_T$  vs  $E_t$  curve at  $|E_b| = 0.4$  V is ca. 20.

Unlike in case of constant bias mode, it is not possible to derive simple diagnostic relations between the characteristic features of the experimental curve and the model parameters. Thus, we compared the full master eq 5 to our experimental data after subtraction of the linear response contribution due to direct tunneling. The baseline was evaluated by the extrapolation of the linear part of the experimental curve. This approximation neglects the different electronic transmission of  $V^{2+}$  and  $V^{+•}$  in the respective off-resonance states and attributes the observed effect to redox-mediated tunneling only.

The resulting theoretical curve is shown in Figure 9; its parameters are shown in Table 2. Similarly as for constant bias mode (cf. section 4.3), the estimated value of  $\xi$  is close to 1. The estimated value of  $\lambda \approx 0.2$  eV is also in agreement with the one obtained from constant bias spectroscopy when starting the trace in the stability range of the  $V^{2+}$  form (Table 2). In contrast,  $\gamma \approx 0.4$  is smaller than obtained before.

The experimental data plotted in Figure 9 do not provide a clear trend at  $E_t < -0.60$  V for  $V^{2+} \rightleftharpoons V^{+•}$  due to the onset of the second redox process  $V^{+•} \rightleftharpoons V^0$ . The extrapolation of the simulated curve toward higher bias values (inset in Figure 9)

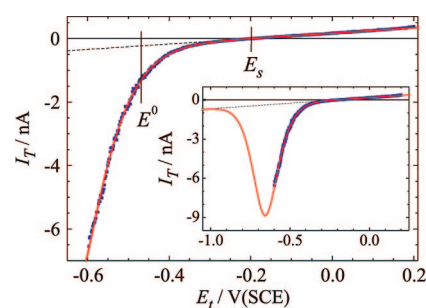


**Figure 9.**  $I_T$  vs  $E_t$  curve recorded in variable bias spectroscopy mode (points), an expected linear current response of the direct tunneling (dashed line), and a fit of the tunneling enhancement (eq 5, solid curve). The inset shows the same data and a simulated curve in a wider potential range assuming that the 2-step ET model with partial vibrational relaxation is valid.

**Table 2.** Estimated Values of the Model Parameters

mode	constant bias		variable bias
	$V^{2+}$	$V^{+•}$	$V^{2+}$
$\lambda$ /eV	$0.2 \pm 0.05$	$0.4 \pm 0.05$	$0.2 \pm 0.03$
$\xi$	0.7–1	0.7–1	$1 \pm 0.03$
$\gamma$	0.85–1	0.85–1	$0.4 \pm 0.03$

demonstrates a maximum of the enhancement current, which reaches zero at  $E_t \ll E^0$ . This, however, does not have a physical meaning but merely reflects the breakdown of the condition  $|E_b| < \lambda$ , required for the validity of eqs 2 and 3. The correct treatment of this situation predicts a constant value of  $I_{\text{enh}}$ .<sup>64</sup>

## 5. General Comments and Conclusions

We carried out current–voltage EC STS experiments in an asymmetric configuration and demonstrated that the experimental observations can be represented by the KU model of a two-step ET with partial vibrational relaxation.

The values of the model parameters  $\xi$  and  $\gamma$ , as obtained from constant bias spectroscopy, are close to 1 independent of the starting potential (Table 2). This result implies that the effective potential at the active viologen core is close to  $E_t$ .<sup>59</sup> A possible physical interpretation of such a result is that the potential profile inside the tunneling gap drops significantly at the substrate and remains rather constant up to the position of the tip. A more complicated picture arises when considering the effect of “Debye screening”.<sup>64,99–101</sup> This effect is expected to be stronger at high electrolyte concentrations, which corresponds to our experimental conditions (0.5 M LiClO<sub>4</sub>). However, it is not clear at the moment, what could be the effect of the ionic components of the monolayer ( $V^{2+}$  respective  $V^{+}$  and coadsorbed ClO<sub>4</sub><sup>−</sup> ions, which replace the Br<sup>−</sup>)<sup>88</sup> as well as of the alkyl spacers on the potential distribution in the gap.

The analysis of the  $I_T$  vs  $E_t$  traces recorded in variable bias spectroscopy mode (Figure 9) yield  $\xi \approx 1$ , while  $\gamma$  is estimated to be ca. 0.4. The former value corresponds to an estimate of the effective potential at the central viologen core of  $E_s + 0.4E_b$  and may reflect an asymmetry in the experimental realization of this mode: the substrate potential  $E_s$  was fixed, while the tip potential  $E_t$  was driven toward rather high values of the bias voltage compared to the experimental conditions applied in constant bias mode spectroscopy. This result agrees with the decrease of both  $\xi$  and  $\gamma$  upon the increase of  $E_b$  in constant bias mode (Table 1).

The reorganization energy  $\lambda$  was found to depend only on the initial oxidation state of the viologen unit and, independent of the chosen spectroscopic mode, is close to 0.2 eV for  $V^{2+}$  and 0.4 eV for  $V^{+}$  (Table 2). We attribute this observation to the aforementioned lowering of the effective tunneling barrier at the interface when a SAM of HS6V6 was electrochemically tuned from the  $V^{2+}$  to the  $V^{+}$  state. In STM experiments, the tip–substrate separation was controlled via a tunneling current feedback loop. The tunneling resistance, rather than a junction geometry, was kept constant upon modification of the redox state of the viologen moiety. In consequence, a wider tunneling gap between tip and substrate is expected for the more conductive  $V^{+}$  adlayer. The effect of a confined tunneling gap on  $\lambda$  was addressed theoretically. Qualitatively, the smaller gap results in a smaller value of the environmental reorganization energy due to the squeezing out of water molecules from the immediate surrounding of the redox center, which is in agreement with our observations.

Our experimental data cannot be represented by a model based on “bare” resonant tunneling<sup>59,66–68</sup> or a vibrationally

coherent two-step ET regime<sup>98</sup> because the position of the maximum of the enhanced tunneling current,  $E_{\text{peak}}$ , is rather close to the formal potential  $E^0$  at low bias voltages. Considering the estimated values of the reorganization energies  $\lambda$  varying between 0.2 and 0.4 eV, the experimentally observed values of  $E_{\text{peak}}$  are significantly different from  $E^0 + 0.2$  (or 0.4) V. These values are predicted by the other two models. The experimentally observed magnitude of the enhanced tunneling current also implies that the model of two-step ET with complete vibrational relaxation does not represent the investigated system properly.

Despite this success, there are also inherent limitations in the chosen model. The derivation of eqs 4–8 is based on the assumption of a strong electronic coupling of the molecule to both electrodes, as reflected in the electronic transmission coefficient  $\kappa \approx 1$ . This boundary condition is not strictly fulfilled in the present case. The tip is separated from the redox-active center not only by the “chemical” barrier of the alkyl spacer, but also by the “tunneling” barrier of the medium. It is possible to account for this asymmetry within the frame of the same model,<sup>58</sup> but this correction does not seem to improve the description of our experimental data significantly.

Another critical point is the estimated absolute value of the pre-exponential factor  $A = e^2 \kappa \rho \omega / (4\pi)$  (eq 5), which corresponds to the adiabatic limit of each of the two ET steps. This is most probably not exactly the case in the present experimental situation. The estimated value of  $A$  corresponds to the ET mediation by a single redox-active center only. This does not imply that exclusively one redox group is trapped in the tunneling gap, but rather that at every moment only one redox center experiences a favorable fluctuation. The scatter between individual measured scans is rather high, and the averaged data represent only a statistical picture. These curves may correspond to  $n > 1$  simultaneously acting mediators. Taking into account the geometry of the tunneling junction, it is difficult to expect that  $n$  is higher than ca. 10. Fortunately, the overestimation of the transmission coefficient and the underestimation of the number of active centers in the tunneling junction are compensating factors.

The robustness of the model and of the analysis presented to the variation of  $A$  is, in addition, supported by the pronounced exponential-type dependence of the resonant current on the reorganization energy  $\lambda$ . The latter contrasts to the proportional dependencies of  $A$  on  $\kappa$  and  $n$ . The effect of possible corrections taking into account more precise values of  $\kappa_1$ ,  $\kappa_2$ , and  $n$  is nearly negligible compared to the error margins of the results extracted from the experimental data.

The real limits of the model are reached in tunneling experiments at high bias potentials  $E_b$ . If the numerical values of  $E_b$  are comparable or higher than  $\lambda$ , the presented version of the model is not adequate anymore. For example, in the constant bias spectroscopy mode a plateau is expected on top of the peak in the limit of  $\lambda \ll E_b$ .<sup>59</sup> Some of our experimental curves, recorded at  $E_b = 0.2$  V under conditions corresponding to  $\lambda = 0.2$  eV (Table 2), indeed demonstrated similar features. However, we did not explore this issue in detail. More critical in this respect are experiments in variable bias mode. The current in the experimentally accessed bias range is well described by the presented version of the KU model. According to the more detailed theoretical simulations, a peak or a plateau in the  $I$ – $E_b$  curves may be observed depending on the properties of the system.<sup>92</sup> Only further experiments with redox-active systems giving access to clear-cut data for a well-defined single redox process at  $E_b > \lambda$  could clarify these issues. The viologen system

(99) Kornyshev, A. A.; Kuznetsov, A. M.; Ulstrup, J. *Proc. Natl. Acad. Sci. U.S.A.* **2006**, *103*, 6799–6804.

(100) Kornyshev, A. A.; Kuznetsov, A. M. *ChemPhysChem* **2006**, *7*, 1036–1040.

(101) Kornyshev, A. A.; Kuznetsov, A. M. *Electrochem. Commun.* **2006**, *8*, 679–682.

exhibits a limitation here due to the non-negligible contributions of a second redox process ( $V^{2+} \rightarrow V^{+}$ ).

Despite this limitation, we stress that with the experimental data available for the viologens, a unique possibility arises for comparing ET characteristics at the single molecule level in a symmetric<sup>39,42,47,48</sup> and an asymmetric configuration. The intriguing question to be addressed is, why electrochemical gating leads to the “switching” of the junction conductance between a low ( $V^{2+}$ ) and a high ( $V^{+}$ ) conductance state in the first case and a redox-mediated maximum in the enhanced tunneling current in the second case.<sup>92</sup> Clearly, the correct answer is based on properties of the nuclear subsystem and the coupling of the tunneling electrons with molecular vibrations. We tentatively attribute the sigmoid increase of the molecular conductance current in the symmetric tunneling junction Au|HS6V6SH|Au to the higher electron density and the higher conjugation of the radical cation molecular wire as compared to the dication bridge. This view is supported by force field calculations of Hesters et al.<sup>102</sup> These authors reported that the interring bond order increases when the viologen dication transforms into the radical upon reduction, which implies that the aromatic character extends across both rings for the latter. The latter also leads to a reduction of the tunneling barrier height as it is observed experimentally in the asymmetric tunneling junction Au|HS6V6|Au under “off-resonance” conditions

(Figure 5). On the other hand, we believe that the enhanced tunneling resonance as observed and quantitatively modeled in the present paper for an asymmetric tunneling junction is dominated by the dynamics of the solvent in the gap. These contributions appear to be significantly smaller in a symmetric junction with individual alkanedithiol-terminated viologen moieties chemically bound to both metal contacts.

We notice that the concept of “soft gating”, as recently proposed by Ulstrup et al.,<sup>48</sup> is an example of the theoretical treatment of ET, deeply rooted in the nuclear motion modes of molecular assemblies. Deeper insight in the redox-molecule mediated junction characteristics are also expected from ab initio based electronic structure simulations combined with transport calculations, such as those attempted in ref 91. Indeed, there are still many other interesting properties of redox-active molecular assemblies in a confined metal|molecule|metal configuration, which still will need to be explored experimentally and theoretically.

**Acknowledgment.** This work was supported by the HGF Project “Molecular Switches”, the DFG, the Volkswagen Foundation, Research Center Jülich, and University of Bern. I.V.P. acknowledges support of DAAD for a Ph.D. fellowship. The viologen derivatives were synthesized by A. Błaszczyk and M. Mayor. We also acknowledge discussion with A. Kuznetsov, J. Ulstrup, M. Ratner, S. Lemay, M. Mayor, A. Bagrets, and F. Evers.

(102) Hester, R. E.; Suzuki, S. *J. Phys. Chem.* **1982**, 86, 4626–4630.

JA8054194